The Astrophysical Journal, 650:484–496, 2006 October 10
© 2006. The American Astronomical Society. All rights reserved. Printed in U.S.A.

THE CHALLENGES OF CORONAGRAPHIC ASTROMETRY[1]

Andrew P. Digby,[2] Sasha Hinkley, Ben. R. Oppenheimer, and Anand Sivaramakrishnan[3]
Department of Astrophysics, American Museum of Natural History, Central Park West at 79th Street, New York, NY 10024; apd@amnh.org, bro@amnh.org

James P. Lloyd[3]
Astronomy Department, Cornell University, 230 Space Sciences Building, Ithaca, NY 14853

Marshall D. Perrin[3,4]
Department of Astronomy, University of California, 601 Campbell Hall, Berkeley, CA 94720

Lewis C. Roberts, Jr.
The Boeing Company, 535 Lipoa Parkway, Suite 200, Kihei, HI 96753

Rémi Soummer[2] and Douglas Brenner
Department of Astrophysics, American Museum of Natural History, Central Park West at 79th Street, New York, NY 10024

Russell B. Makidon[3]
Space Telescope Science Institute, 3700 San Martin Drive, Baltimore, MD 21218

Michael Shara
Department of Astrophysics, American Museum of Natural History, Central Park West at 79th Street, New York, NY 10024

Jeffrey Kuhn
Institute for Astronomy, University of Hawaii, 2680 Woodlawn Drive, Honolulu, HI 96822

James Graham[3] and Paul Kalas[3]
Department of Astronomy, University of California, 601 Campbell Hall, Berkeley, CA 94720

and

Laura Newburgh
Department of Physics, Columbia University, 538 West 120th Street, New York, NY 10027
Received 2005 December 7; accepted 2006 May 31

ABSTRACT

A coronagraph in conjunction with adaptive optics provides an effective means to image faint companions of nearby stars from the ground. The images from such a system are complex, however, and need to be fully characterized and understood before planets or disks can be detected against the glare from the host star. Using data from the Lyot Project coronagraph, we investigate the difficulties of astrometric measurements in diffraction-limited coronagraphic images and consider the principal problem of determining the precise location of the occulted star. We demonstrate how the image structure varies when the star is decentered from the optical axis and show how even small offsets ($0.05\lambda/D$ or 5 mas) give rise to false sources in the image. We consider methods of determining the star position from centroiding, instrument feedback, and analysis of point-spread function symmetry and conclude that internal metrology is the most effective technique.

Subject headings: astrometry — instrumentation: adaptive optics — methods: data analysis — planetary systems — techniques: high angular resolution — techniques: image processing

Online material: color figures

1. INTRODUCTION

Since the first discoveries of extrasolar planets a decade ago (Mayor & Queloz 1995; Marcy & Butler 1996), there have been increasing efforts to image planets orbiting nearby stars. The main obstacle to achieving this aim is the scattered light from the parent star, which renders any adjacent planet invisible to conventional imaging instruments. Adaptive optics (AO) coronagraphy (Nakajima 1994; Sivaramakrishnan et al. 2001) attempts to circumvent this problem by using a high-order AO system to control the wave front and concentrate the starlight into a diffraction-limited core, and then use a coronagraph to suppress diffracted light from the field of interest surrounding the star. In this way large flux contrast ratios (or dynamic ranges) are attainable, enabling the detection of faint objects such as brown dwarfs, disks, and exoplanets orbiting the target star.

Recent results from the Lyot Project[5] (Oppenheimer et al. 2004) have demonstrated that high dynamic ranges at close separations are achievable with current AO coronagraphy (Hinkley et al. 2006). The contrasts attained are sufficient to put large hot Jovian planets within direct detection limits today, providing present AO coronagraphs with the potential to yield exciting

[1] Based on observations made at the Maui Space Surveillance System operated by Detachment 15 of the US Air Force Research Laboratory's Directed Energy Directorate.
[2] Michelson Postdoctoral Fellow.
[3] NSF Center for Adaptive Optics.
[4] Michelson Graduate Fellow.
[5] See http://www.lyot.org.

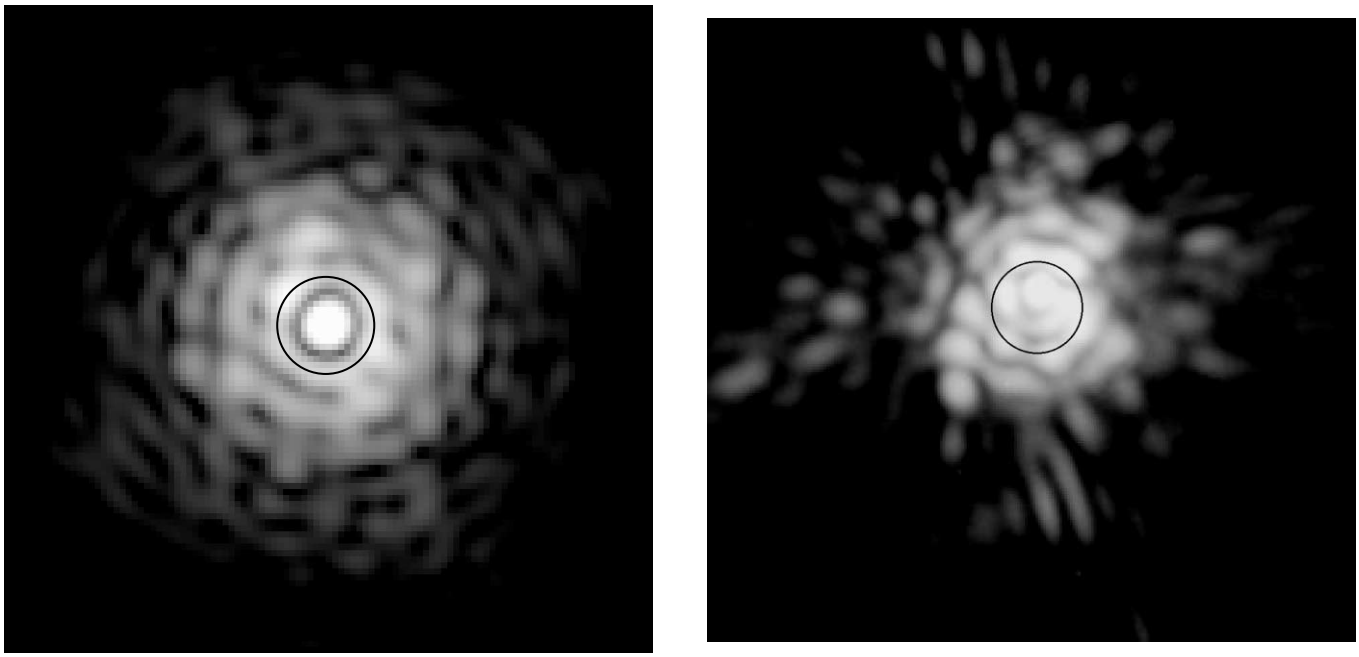

FIG. 1.—Simulated (*left*) and observed (*right*) PSFs of the Lyot Project coronagraph on the AEOS telescope. Note the presence of pinned speckles in the observed data and the "spider" cross pattern caused by diffraction from the telescope secondary mirror support structure (not included in the simulation). In both images the circle represents the locus of the coronagraphic spot, and the intensity scale is logarithmic.

discoveries of faint companions. These instruments are also valuable test beds for understanding the issues faced by future, even more ambitious experiments, such as the *Terrestrial Planet Finder* (Stapelfeldt et al. 2005) and "extreme" AO systems on large ground-based telescopes (e.g., Macintosh et al. 2004).

An important aspect of these studies is the astrometry of coronagraphic images. Precise measurements of the position of a putative companion relative to its host star are crucial in establishing physical association and in determining its orbital characteristics. Knowledge of the exact location of the star in the image is also important for reduction and analysis purposes. Over a long exposure objects are "smeared" by slow drifts in the AO system, differential refraction, and field rotation, and the image is further complicated by the presence and random motion of speckles (§ 2). These time-dependent effects, combined with the dynamic range limit of the detector, prevent long integration times and require many short exposures to be summed to provide a deep image. These single frames, with integration times of $\sim$10–20 s in Lyot Project observations, need to be registered to each other before they can be summed. However, this registration is not easy in the presence of field rotation and motion in narrow-field images where there is often no object to use as a reference point other than the target star itself.

Furthermore, in coronagraphic images the star is occulted, so its location cannot be determined in a straightforward manner. In addition, AO coronagraphic images have highly complicated point-spread functions (PSFs), and so the important task of measuring astrometry becomes a considerable challenge.

2. SIMULATED AND OBSERVED AO CORONAGRAPHIC IMAGES

The theoretical PSF of an AO telescope with an annular aperture and without a coronagraph exhibits a clean diffraction pattern with unbroken Airy rings visible to large radii. In the absence of wave front aberrations the position of the star is therefore aligned with the center of the symmetric PSF, and this symmetry is preserved when a perfect coronagraph is introduced to the beam path. This is not the case in observed images, however, which suffer aberrations that distort the ideal PSF. The presence of tilt in the wave front, for example, leads to the appearance of "fake sources" in the image, which results in the star position not corresponding to the image plane peak intensity. This is predicted by Lloyd & Sivaramakrishnan (2005) and confirmed by the results presented in this paper.

Observed AO images are also dominated by speckles: constructive interferences of uncorrected components of the stellar wave front arising from optical imperfections and atmospheric variability. These PSF fluctuations dominate photon noise and, owing to their source from atmospheric fluctuations and fixed and moving optics, create a variable background halo that significantly limits the potential dynamic range of the image (Racine et al. 1999; Bloemhof et al. 2001; Aime & Soummer 2004). The image is further distorted by first-order speckles that are "pinned" to the inner Airy rings and, due to antisymmetry, have corresponding "dark" speckles at the opposite point of the ring (Bloemhof et al. 2001; Sivaramakrishnan et al. 2002; Bloemhof 2003; Perrin et al. 2003b). These antisymmetric pinned speckles may also be misinterpreted as real astronomical sources in coronagraphic data (Bloemhof 2004).

Recent simulations of AO coronagraphic images attempt to incorporate these imperfections by assuming an imperfectly corrected wave front and by modeling the true PSF as a halo of speckles around a diffraction-limited core (Perrin et al. 2003b). Further wave front errors such as the "waffle mode" of the AO system are also added (Makidon et al. 2005), resulting in a prediction that can resemble the observed image more closely than simple idealized simulations.

A result of uncorrected wave front aberrations and speckles is that the intensity center of the Airy pattern will not correspond to the star position in the image. Determining the occulted star position in coronagraphic images is important, yet despite the accuracy of the simulations, they do not consistently match the observations accurately enough for this purpose. Although some wave front errors are included in the simulations, it is difficult to

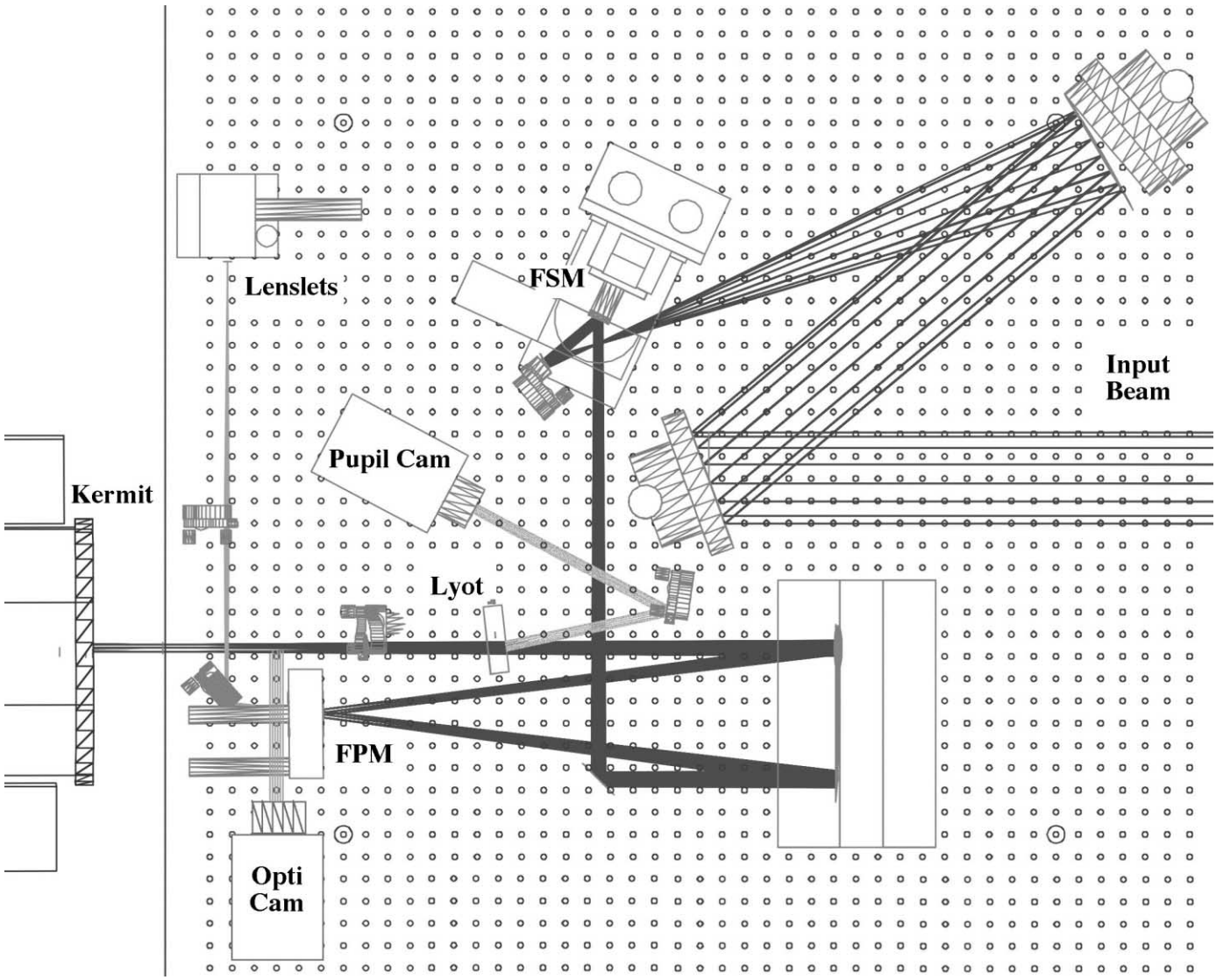

FIG. 2.—Ray-trace diagram of Lyot Project coronagraph. The FSM and lenslets form part of the tip-tilt loop described in the text.

incorporate into the models the highly variable AO correction and the complex optical imperfections of the telescope and instrument. The approximation of the PSF as a diffraction-limited core plus a speckle halo provides further discrepancies between the simulated and real images, as do other unpredictable effects such as diffracted light from the telescope spiders appearing due to small optical misalignments (Fig. 1). These unmodeled components all add unknown distortions to the symmetry of the image and therefore contribute to the spatial discrepancy between the actual star position and the estimated intensity centroid. Image asymmetries also arise from astronomical sources in the field: light from circumstellar disks, companions (both seen and unseen), and background objects may provide further inseparable complications to the image structure.

The final coronagraphic image is therefore affected by many uncertainties arising from optical imperfections, atmospheric variability and true sources adjacent to the star. These all result in a departure from a perfectly symmetric image and make determination of the occulted target star position difficult, even with sophisticated simulations. This problem must therefore be addressed empirically as well as theoretically, and given the importance of accurate astrometry in searching for disks and companions, it is an issue that is significant for not only the current but also the next generation of coronagraphs.

3. THE LYOT PROJECT

The Lyot Project is an experiment aimed at the direct imaging of faint companions and disks around nearby stars. It features a diffraction-limited, optimized Lyot coronagraph (Lyot 1939) used in conjunction with the "Kermit" infrared camera (Perrin et al. 2003a). It is deployed at the 3.63 m Advanced Electro-Optical System (AEOS) telescope on Haleakala at the Maui Space Surveillance System. The project utilizes the 941-actuator AO system on AEOS (Roberts & Neyman 2002), one of the highest order AO systems in operation. The coronagraph (Fig. 2) includes a number of novel capabilities, such as active pupil alignment and simultaneous dual-band imaging, and also features a high-speed tip-tilt loop to compensate for image motion. A full description of the coronagraph can be found in Oppenheimer et al. (2004), but here we summarize the design of the tip-tilt control loop, which is of particular relevance to this study.

The first stage of the tip-tilt loop (Fig. 3) is a fast steering mirror (FSM) that maintains star alignment with the occulting spot, which is a hole in the focal plane mask (FPM) mirror. Four

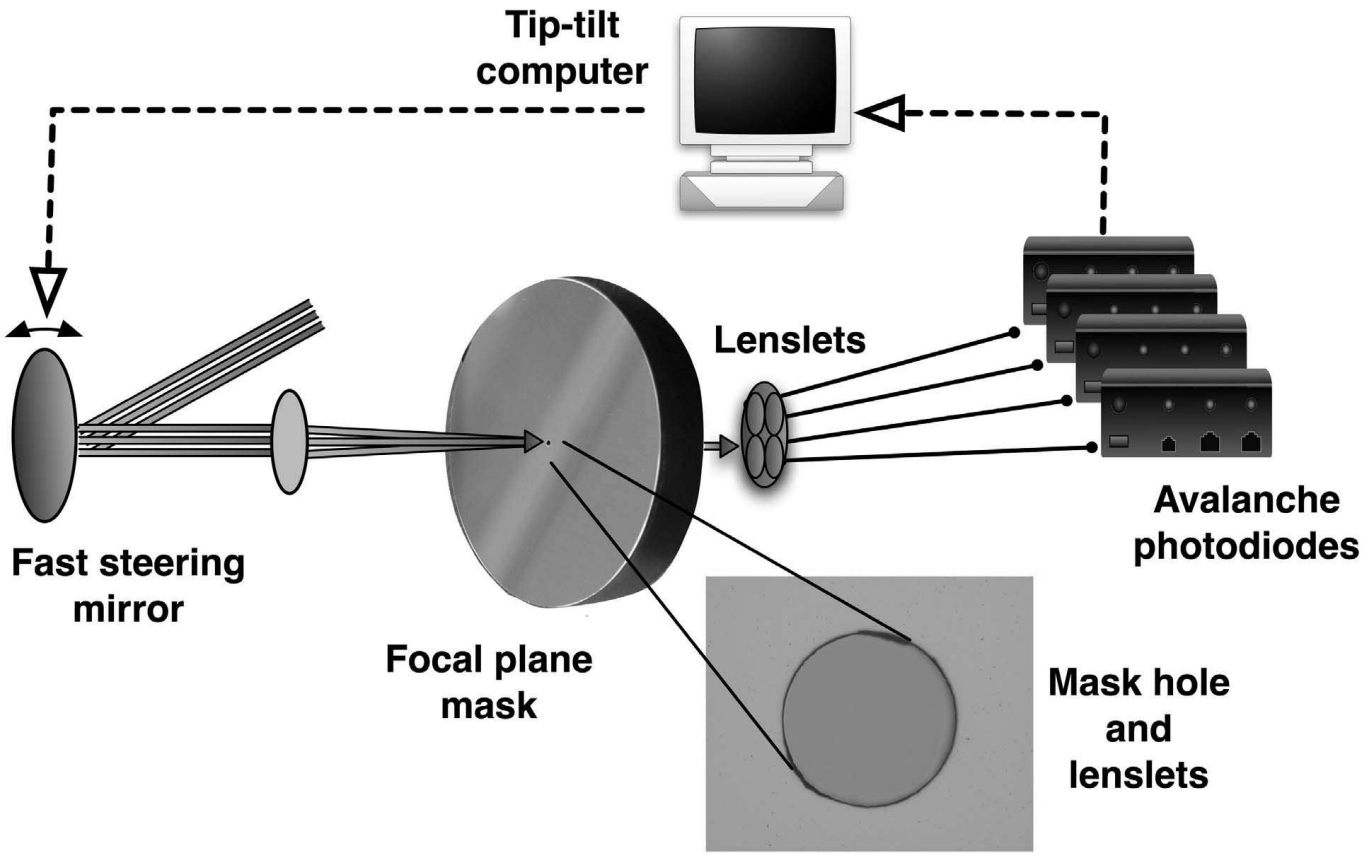

FIG. 3.—Schematic diagram of the coronagraph tip-tilt loop. Four lenslets are mounted on a fiber head behind the hole in the focal plane mask, which serves as the coronagraphic occulting spot. Star light passing through this hole reaches the lenslets, and the photons incident on each lenslet are counted by APDs, which pass the counts to the tip-tilt computer. The computer calculates the star center from the count signal to determine the location of the star with respect to the focal plane hole and then drives the FSM to keep the beam centered on the hole. The whole tip-tilt loop operates at a frequency of up to 1 kHz.

lenslets situated on a fiber head behind the occulting stop feed star light passing through the mask hole to photon counting modules (avalanche photodiodes, or APDs) connected to the tip-tilt computer. This computer determines the position of the star relative to the occulting spot from the centroid of the counts and adjusts the alignment accordingly by altering the angle of the FSM. This whole process operates at high speeds, with update rates of up to 1 kHz. The beam can be driven to any position within the focal plane hole by moving the lenslets, which are mounted on an *xy* motorized stage parallel to the mask plane. In principle the lenslet motor positions can therefore be used to infer the position of the occulted star relative to the mask hole (§ 5.1).

4. CORONAGRAPHIC PSF AS A FUNCTION OF TILT

4.1. *Method*

The Lyot Project coronagraph and camera provide *H*-band images with Strehl ratios of up to 85% and very high dynamic ranges. These images form an ideal basis with which to compare coronagraphic theory and simulations with real observations. During each observing run images of binary stars are taken for instrument calibration purposes; these are also useful for studying astrometry in coronagraphic images. The data used in this paper are from observations of the binary stars HIP 62886 and HIP 25813, taken at epochs 2005.060 and 2005.065, respectively. Table 1 gives the discovery designation and Tycho magnitudes (Fabricius & Makarov 2000) of these stars, as well as the separations and position angles of the binary components at the epoch of observation, as calculated from their orbits. The orbits of HIP 25813 and HIP 62886 are given by Seymour & Hartkopf (1999) and Heintz (1997), respectively.

To investigate the PSF structure as a function of the position of the star behind the occulting mask, the primary star of the binary system was placed behind the spot with the coronagraph tip-tilt loop activated, and about 50 exposures were taken with the star in different positions behind the mask. The star was moved by altering the position of the tip-tilt loop lenslets by $\sim$20 μm at a time, which corresponds to $\sim$1.5 pixels in the image (the pixel scale is $\sim$13.5 mas pixel^{-1}). In this way the star was decentered by up to $\sim$230 mas or $\sim 2.5\lambda/D$ from the spot center (where λ is the wavelength of observation and D is the diameter of the telescope primary mirror); a substantial area of the occulting mask was therefore explored. The occulting spot diameter was 450 μm ($5.3\lambda/D$ at 1.65 μm *H*-band wavelength), and the Lyot stop had a clear annulus between radii of 0.644 and 1.407 m, as projected onto the 3.63 m primary telescope mirror. This corresponds to a Lyot stop tuning parameter (Sivaramakrishnan et al. 2001) of $\mathcal{F} = 0.6$, where $\mathcal{F}$ defines the fractional radial undersizing of the Lyot stop.

TABLE 1
BINARY CALIBRATION STARS

Name/Designation	V_T(A)	V_T(B)	ρ (arcsec)	θ (deg)
HIP 25813/STF 1687 AB.....	4.47	5.79	1.22	45.4
HIP 62886/STF 728.....	5.17	7.17	1.04	190.0

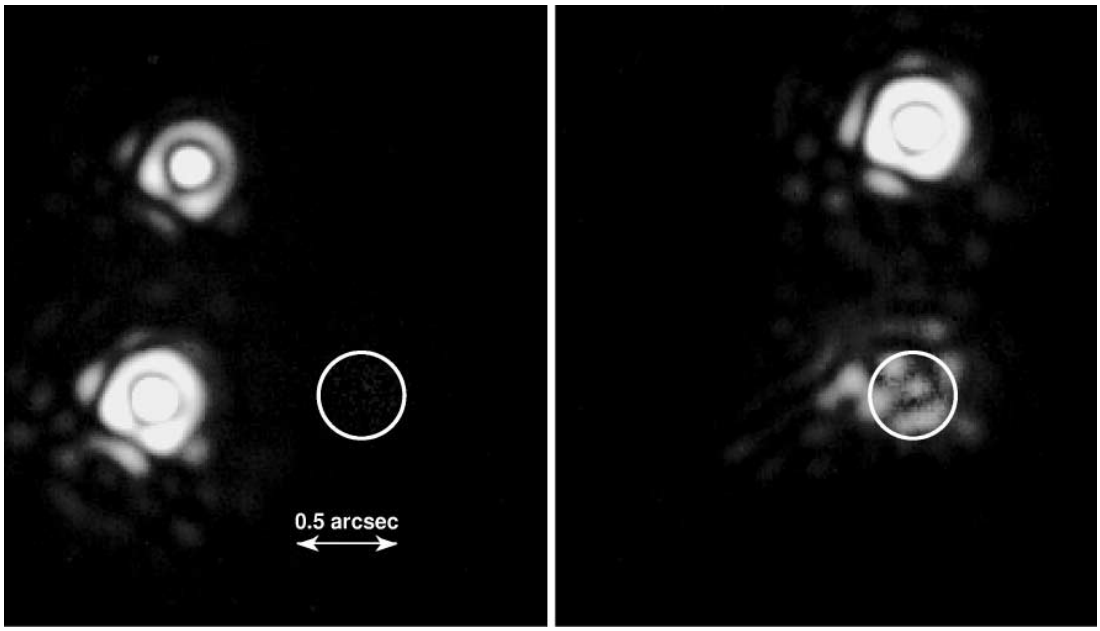

FIG. 4.—Unocculted (*left*) and occulted (*right*) images of the binary star HIP 25813, with the circle denoting the location of the coronagraphic spot. Unocculted images showing both components of the binary systems are used to infer the location of the hidden star in occulted images, as described in the text. [*See the electronic edition of the Journal for a color version of this figure.*]

The exact location of the occulted primary star was inferred from its unocculted binary companion as follows. A series of unocculted images of the binary system was taken (Fig. 4), and the position of the two stars in each image was found from PSF fitting using the IRAF DAOPHOT package (Stetson 1987, 1992). The determination of stellar positions in AO images is fraught with difficulties (see, e.g., Anderson & King 2000; Mighell 2005), and so other deconvolution techniques of determining the precise star position were considered (see discussions in Christou et al. 2004; Véran & Durand 2000). However, these methods were found to be not suitable for our large and sparsely populated stellar images. Furthermore, alternative techniques produced essentially identical positions at the level of accuracy required in this study. Star positions determined by DAOPHOT PSF fitting differ from those calculated from the centroids of best-fitting Gaussian functions by a mean of less than 0.1 pixels ($\sim$1.5 mas), which is negligible compared to other sources of error (§ 5.1.1).

Using DAOPHOT, a mean PSF was determined from unocculted observations of a known single star taken prior to the binary exposures. This empirical PSF was then fitted to the unocculted binary images by an iterative least-squares method to yield x- and y-coordinates for each binary star, and the vector between them was calculated. Since the Lyot Project coronagraph is at a coudé focus of an Alt-Az telescope, the secondary-primary vector was derotated to a reference frame in which north is aligned with the image y-axis and east with the negative x-axis. The mean derotated vector from the secondary star to the primary was then calculated from all of the unocculted binary system images. With this a priori information of the vector of the primary star from the secondary, the location of the primary in any occulted image could then be deduced from the position of its companion, assuming a uniform plate scale across the field of view. This assumption is acceptable for this study, since distortions arising from spatial irregularities in the infrared camera array structure and from the camera and coronagraph optics are predicted to be less than 2 μm (1.5 mas), even at large separations (>2.″7). The distortions from the AEOS telescope are 60 mas over a 36″ field of view and so will be on the order of a few milliarcseconds over the field angles of the data used in this study. The expected total field distortion is therefore small compared with other sources of astrometric error (§ 5.1.1).

4.2. *Results*

The changes in the image structure arising as a result of the occulted star being moved with respect to the coronagraphic spot are demonstrated qualitatively in Figure 5. The circle denotes the estimated locus of the $5.3\lambda/D$ (450 mas) diameter occulting spot, predicted from a flat-field image, and the dot shows the location of the occulted star estimated from the binary companion by the method described in § 4.1. Light leaks into the image region occulted by the coronagraphic mask due to diffraction and appears in the images as Airy rings with either a bright or dark central spot. A "ghostly PSF" is predicted to form on-axis as a result of second-order tilt and first-order defocus effects (Lloyd & Sivaramakrishnan 2005; Sivaramakrishnan et al. 2005), and this combines with the PSF of the star to produce the complex structure seen in Figure 5.

4.2.1. *Fake Sources*

It is noticeable that the star location does not always coincide with the intensity peak inside the occulting spot, and particularly significant are the fake sources that appear at the edge of the spot toward which the star is moved. These sources are predicted in Lloyd & Sivaramakrishnan (2005) and are expected to appear at large tilts, when the star is less than one diffraction element ($1\lambda/D$) from the edge of the spot. Our data, however, show that they are prominent even when the star is decentered by small amounts (less than $0.5\lambda/D$ from the spot center, or more than $2.0\lambda/D$ from the spot edge).

The formation of the fake sources with increasing tilt is demonstrated quantitatively in Figure 6, which shows the image and corresponding radial profile counts when the star is moved from the x-center of the spot toward the edge. While the flux inside the mask domain remains approximately constant, the source just outside the spot boundary grows brighter as the star approaches. The magnitude of the sources may be exaggerated by aberrations

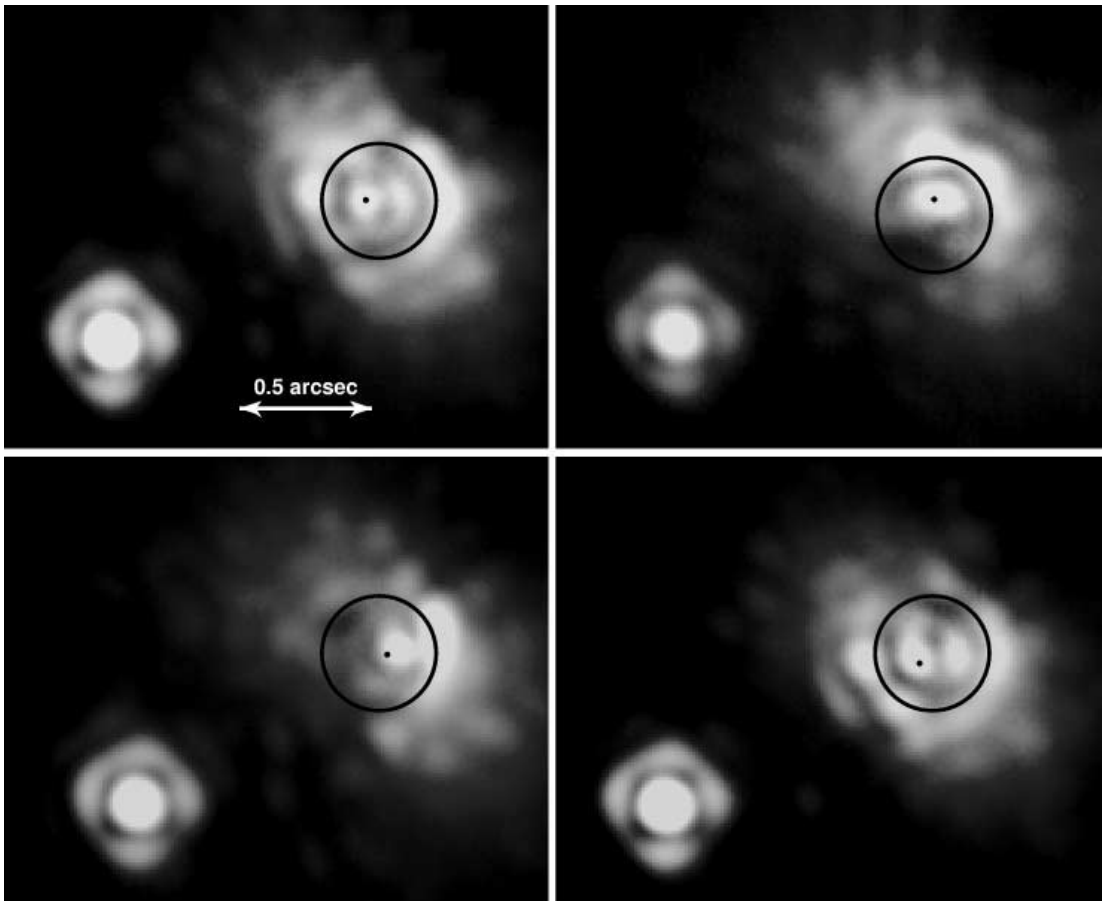

FIG. 5.—Changes in the coronagraphic image as a function of the star position (*dot*) behind the occulting spot (*circle*). The position of the occulted star is inferred from the binary companion, and the spot locus is estimated from a flat-field image. The (x, y) star offsets from the center of the 450 mas diameter spot are (*clockwise from top left*, in mas) $(-51.2, 1.3)$, $(-1.0, 56.9)$, $(30.3, -6.3)$, $(-49.6, -39.4)$. The fake sources appearing at the edge of the spot when the star is decentered are clearly visible in these images. The intensity scale is logarithmic. [*See the electronic edition of the Journal for a color version of this figure*.]

other than tilt, or by errors in the estimated mask and star positions, but the appearance of the fake sources predicted in Lloyd & Sivaramakrishnan (2005) is nevertheless confirmed by these data. There is also little doubt that even small changes in the position of the star behind the mask result in significant variations of the PSF structure.

The relative "roundness" of the focal mask hole is also relevant to PSF structure, since light scattered from machining imperfections in the mask perimeter may appear in the image. With a pixel scale of 13.5 mas and a plate scale at the focal plane mask of 0.940 mas μm^{-1}, such features must be certainly be no larger than ~ 12 μm in the Lyot Project coronagraph if they are not to adversely affect the image. Initial micrographs indicate that the mask defects are smaller than this, but the exact size at which coronagraphic spot irregularities significantly degrade the image will be investigated with further high-resolution microscopy in a future study.

Interpolation of the line profiles shown in Figure 6 suggests that the fake sources become brighter than the light in the spot interior when the star is decentered by more than approximately 5 mas, or $\sim 0.05\lambda/D$. More data are needed in order to accurately quantify this value, and this will be pursued with future calibration observations. The data presented here nevertheless indicate that the star must be positioned to within subpixel precision of the occulting spot center if false sources are not to significantly contaminate the field immediately adjacent to the spot. This is expected to be possible with the Lyot Project coronagraph, since the tip-tilt loop lenslet motors provide a repeatable positioning accuracy of better than $\frac{1}{3}$ pixels (4.5 mas) (§ 5.1.1), and the loop maintains the stability of the star position to 1 mas. This stability is a long-exposure rms sky value and is equivalently 30 μas in the laboratory.

That the fake sources are prominent even at small decenterings reinforces earlier warnings (Krist et al. 1998; Lloyd & Sivaramakrishnan 2005) that care must be taken in high-Strehl coronagraphy not to misinterpret structure close to the spot and to ensure that the fake sources are not mistaken for real ones. This is particularly important in instances when the star is deliberately moved from the spot center, in order to expose a very close companion, or when atmospheric refraction effects (§ 5.1.2) are large, for example. Lower sensitivity to tilt (and other aberrations) can be achieved through the use of novel coronagraph designs rather than the classical Lyot coronagraph with hard-edged occulting stop used here. Such designs employ features such as pupil apodization (Aime et al. 2002; Soummer 2005) and band-limited (Kuchner & Traub 2002) or "eighth-order" (Kuchner et al. 2005; Shaklan & Green 2005) focal plane masks. Despite this, careful characterization and modeling of the PSF at different tilts are necessary irrespective of coronagraphic design, in order not to confuse light leaking around the occulting spot with real astronomical sources. In addition, care must be taken to ensure that antisymmetric pinned speckles are not falsely interpreted as companions in coronagraphic data (Bloemhof 2004).

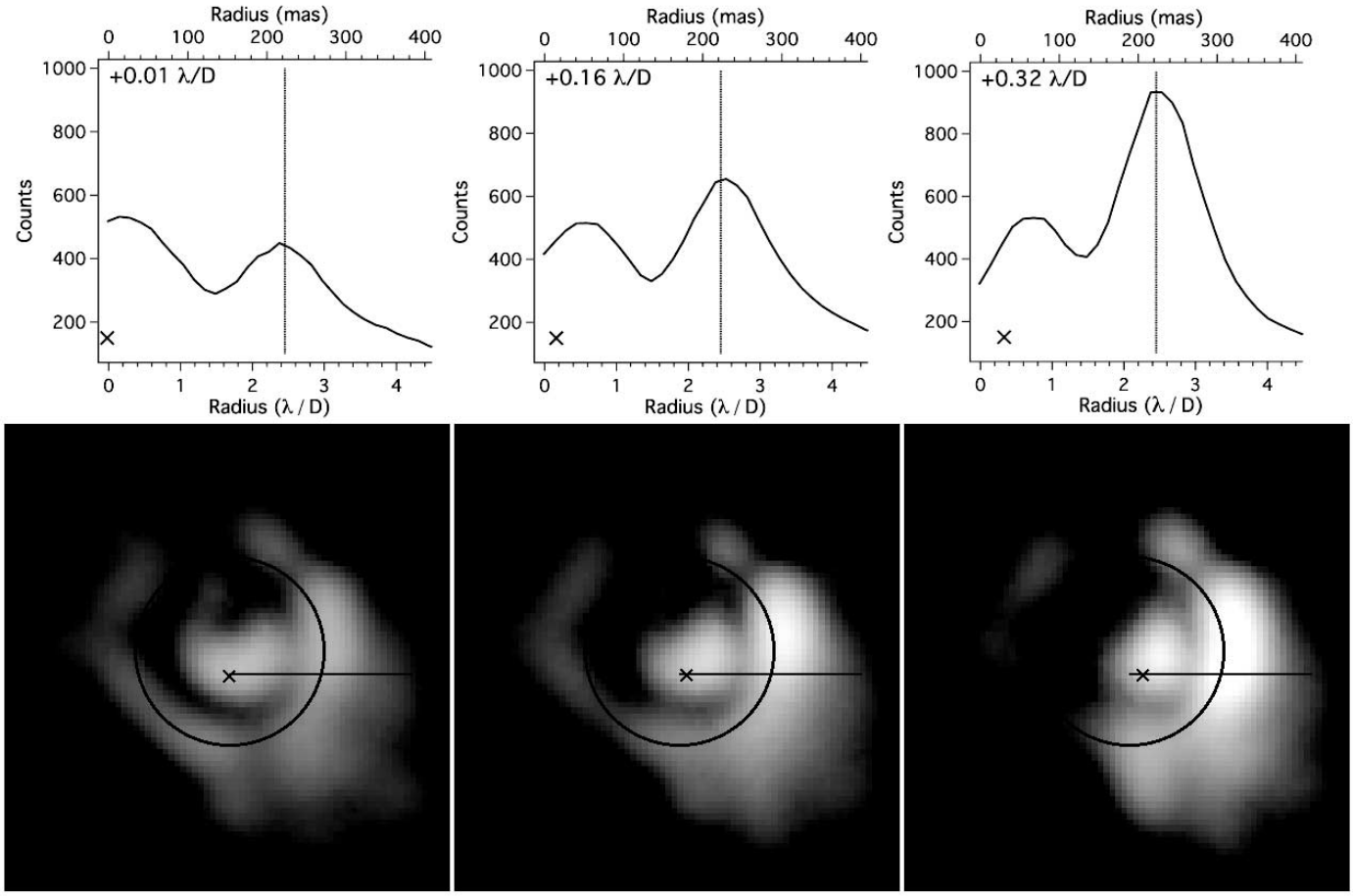

FIG. 6.—Images and radial profiles of the region around the occulting mask, showing the formation of fake sources at the edge of the spot as a function of tilt. In each image the locus of the 450 mas diameter occulting spot (*circle*) and estimated star position (*cross*) are shown, as well as the line along which the radial profile is calculated. The intensity scale is logarithmic. The vertical line in the radial profile plots denotes the edge of the occulting mask, and the cross denotes the distance of the star from the spot *x*-center. As the star is moved from the center of the mask, the flux of the "source" at the edge of the spot increases. The distances by which the star is decentered from the axis are (*left to right*) $-0.02\lambda/D$, $+0.16\lambda/D$, and $+0.32\lambda/D$, or -1.7, 14.5, and 29.1 mas.

4.2.2. *Intensity Centroid*

It is clear even from visual inspection of Figure 5 that the star does not lie at the intensity center of these highly complex images. In order to confirm this, the star position determined from the binary companion was compared with the intensity centroid of the images of HIP 62886 (Fig. 7). The intensity centroid was calculated by

$$(\rho_x,\ \rho_y) = \frac{1}{I_{\text{total}}}\left(\sum_j \sum_i I_{ij} x_i,\ \sum_j \sum_i I_{ij} y_j\right), \qquad (1)$$

where I_{ij} is the intensity of the pixel with coordinates (x_i, y_j) and I_{total} is the total summed intensity. In order to avoid contamination from the companion, only the central 100×100 pixel region of the image was included in this calculation. The positions of the centroid and the binary star for each image were found to be significantly different, with a median discrepancy in *x* and *y* of 74 and 11 mas, respectively (74 mas resultant in both coordinates), for a subimage centered on the occulting spot center.

Figure 7 shows that there is significant discrepancy between the intensity centroid of the image center and the true star position assumed from the binary companion. Furthermore, the derived centroid location is sensitive to the image subregion used, due to the variability of the speckles and telescope spider brightness over the spatial extent of the image. In the absence of sky and readout noise the entire image should ideally be included in this calculation, but this is not possible since the centroid derived from a subregion containing the binary companion (or any other source) would be measured from multiple PSFs and would clearly not coincide with the position of the occulted star. Other sources in the image cannot be removed without precise PSF subtraction, which is difficult to achieve in these AO images.

Even if the removal of other sources could be accomplished, the speckles that are dominant at these high Strehl ratios further complicate the image. They can clearly be seen in the background halo and pinned to the bright Airy rings of Figure 5. Inspection shows that some of the speckles are quite stable over the duration of the observations (about 20 minutes), whereas others have much shorter lifetimes. The unpredictable variability of speckles—a result of whether they arise from imperfections in fixed or moving optics or from atmospheric turbulence—makes their subtraction from an image extremely difficult (e.g., Sivaramakrishnan et al. 2002). Atmospheric turbulence also introduces temporal and spatial errors in stellar positions determined from centroiding (Lindegren 1980; Sivaramakrishnan et al. 1995; Lazorenko & Lazorenko 2004) and will further affect this method.

Therefore, the presence of other astronomical sources (whether visible or not), speckles, atmospheric turbulence, and light diffracted around the telescope spiders all distort the morphology of the occulted image to such an extent that it is extremely difficult to predict the star location from the intensity centroid. That the centroid position is more closely aligned with the true star position

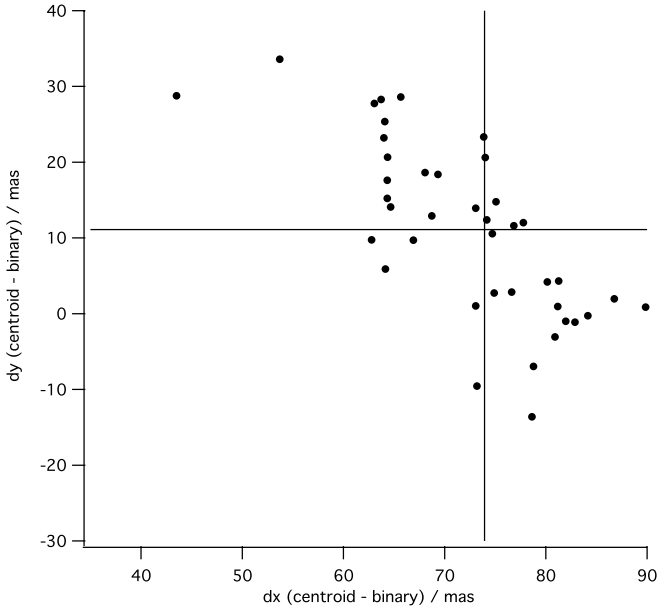

FIG. 7.—Spatial differences between the x- and y-coordinates of the intensity centroid and the star position inferred from the binary companion for images of HIP 62886. The median differences in x and y between the centroid and assumed star position are shown as solid lines. The intensity centroid is a poor indicator of the star position and is also highly dependent on the positioning of the subregion in which the centroid is calculated, due to speckles, atmospheric turbulence, and astronomical sources in the image other than the target star.

in the y-coordinate than in x in the images of HIP 62886 is likely to be due to a combination of all of these effects.

5. SOLUTIONS TO THE "STAR LOCATION" PROBLEM

With many complex distortions of the image it is extremely difficult, if not impossible, to determine the exact location of the star in the image from conventional analysis techniques such as centroiding or PSF fitting. Possible solutions to this important problem can be divided into two broad régimes: those that rely solely on the information contained in the image to recover the star position, and those that use additional information from the instrument configuration.

5.1. *Instrument Feedback*

Estimating the star position from instrument feedback can circumvent the problems arising from the complexity and variability of occulted coronagraphic images. As noted in § 3, the position of the occulted star in an image from the Lyot Project coronagraph can in principle be deduced from the lenslet motor positions. The aim of this is not to achieve accurate centering of the lenslets behind the occulting mask—this is achieved by prior calibration—but rather to recover the star position for the purpose of astrometric analysis of the image.

Although the tip-tilt system used here is unique to this instrument, the principle of using instrument feedback to deduce the star position is applicable to all very high contrast AO coronagraphs. By definition all AO instruments use feedback, and high dynamic range coronagraphs require a precise guidance mechanism to actively maintain alignment with the coronagraphic spot. Feedback from this system can be used to infer the position of the star with respect to the occulting spot and hence the location of the star within the image. While the design of the guidance system will vary between instruments, in this paper we use the Lyot Project coronagraph as an example of the instrument feedback approach for estimating the star position and as a relative measure of its effectiveness when compared to other techniques.

Other methods of determining the star position that are not applicable to this instrument may be considered for some coronagraphs. One such approach is to interleave occulted exposures with integrations in which the coronagraphic mask is removed from the beam path, so that the star position can be measured directly. However, this technique is not possible with the increasing number of coronagraphs (such as the Lyot Project instrument) that use occulted light as feedback to the control loop, since removing the occulting mask would result in disruption of light reaching the tip-tilt sensors. Furthermore, it is likely to prove very difficult to implement in practice, since removing the coronagraphic mask from the beam in between occulted exposures would require extremely precise control of the beam position or focal plane mask. With the majority of tip-tilt systems attaining at best 1 mas rms stability, most instruments would not have the highly accurate beam control necessary to implement this method.

Feedback methods from the tip-tilt loop will suffer from corresponding difficulties in instruments less stable than those at a coudé focus. Coronagraphs on Cassegrain mounts will experience significant flexure problems, for example, which will adversely affect the stability of the beam and attempts to deduce the star position from tip-tilt feedback. However, as a result such instruments will require automated flexure and stability control in order to achieve the high dynamic ranges necessary to detect faint companions. Accordingly, since all high-contrast AO coronagraphs require precise active alignment of the star with the occulting spot, information from a feedback loop will exist irrespective of the instrument and telescope architecture.

With the Lyot Project coronagraph the relation between the lenslet motor positions and star location was investigated with the experiment described in § 4, in which the primary star was moved to different locations behind the mask by adjusting the lenslet motors. The lenslet motor positions are recorded in the FITS header of the images, and these values were compared to the occulted star pixel position estimated from the binary companion.

Results show a good correlation between the lenslet position and image pixel coordinate in x and y (Fig. 8), with residuals of less than 1 pixel (13.5 mas) and no significant correlation between the x- and y-coordinates (Fig. 9). The gradient of the transformation is consistent between observations of different stars, at 0.035 pixels μm^{-1}, and the rms residuals are 0.482 and 0.286 pixels in x and y, respectively. These results suggest that the star location can currently be inferred from the lenslet motor positions to an accuracy of $\sim$10 mas. In the interest of improving this accuracy, we now consider the residual errors in the relation and discuss the differences in the transformation that occur between stars.

5.1.1. *Errors in the Lenslet-Star Position Relation*

There are a number of possible causes of the residual scatter in the lenslet-star position relation: tip-tilt loop errors, motor positioning errors and hysteresis, field distortion, astrometric and field derotation errors, and insufficient correction for atmospheric refraction. Of these, tip-tilt loop and motor positioning errors are unlikely to contribute significantly to the scatter observed in Figure 8, since the tip-tilt loop is stable at the level of 1 mas ($\sim$1/15 pixels), and the motors are engineered to have positioning errors of just 1 μm ($\sim$1/30 pixels) when driven in one direction. It should be noted, however, that the latter uncertainty has not been independently verified in our system and that additional effects such as changes in the APD gains and temperature fluctuations in the instrument will also introduce further errors in the relation between star and lenslet motor positions.

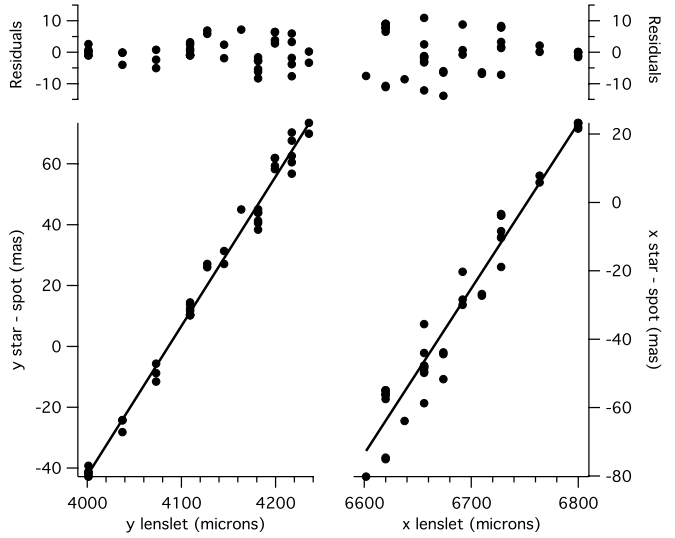

FIG. 8.—Instrument feedback estimates of the occulted star position for HIP 62886, showing the results of changing the star position relative to the occulting spot by moving the motors controlling the tip-tilt loop lenslets. The star positions are relative to the center of the 450 mas diameter spot and show good correlations between the lenslet motor positions and star pixel positions in both x- and y-coordinates. The residuals suggest that the star location can be determined to an accuracy of 1 pixel (13.5 mas) from the lenslet motor readings. The linear correlation coefficients for x and y are 0.975 and 0.995, respectively, and the rms residuals are 0.482 and 0.286. Slight evidence for motor hysteresis can be seen at the lower end of the x lenslet scale.

Motor hysteresis is expected to impart a more significant error of $\sim$10 μm, or $\frac{1}{3}$ pixels, and evidence for this can be seen in the lower part of the x relation in Figure 8. The y lenslet motor appears to be much less affected by hysteresis. Any nonuniformity of the plate scale due to field distortion would also produce deviations from the linear lenslet-star position relation, although given that only a small portion of the detector ($<200\times200$ pixels) was used for this test, this is unlikely to have a significant effect (see § 4.1).

Astrometric errors in the measured star positions will also clearly affect the correlation with the lenslet motor positions. Care has therefore been taken to obtain accurate astrometry with PSF fitting using DAOPHOT, and tests of different fitting methods show mean discrepancies of less than $\sim$0.1 pixels. Scintillation and isoplanatism will also give rise to errors in the derived binary star positions due to the assumption of a spatially and temporally fixed PSF (Roberts et al. 2005 and references therein). Given that these are natural guide star AO observations at relatively long wavelengths, with low zenith distances and long integration times, these effects will, however, be small. Furthermore, the binaries observed have small separations ($\lesssim1''$) compared to the nominal anisoplanatic angle for AEOS (Drummond et al. 2003; Christou et al. 2003; Roberts et al. 2005).

While it is difficult to ascertain the contribution to the total error of each of the possible sources of scatter in the lenslet feedback relation, two of the largest of these are likely to be the inaccuracies in the derotation of the individual frames and the inadequate correction for atmospheric differential refraction. The derotation applied to each image is calculated from a formula derived semiempirically from observations of binary stars with known separations and position angles; the rotation rate is known analytically from the position angle, altitude, and azimuth of the telescope, but the constant rotation offset had to be determined from calibration observations. Errors in this offset will not contribute to the scatter evident in Figure 8, but uncertainties arising from ascribing a single position angle, azimuth, and altitude to each integrated exposure will do so, especially for rapidly rotating fields near the zenith. Comparison of the derived rotated secondary-primary star vectors for different images shows that the errors in the derotation are on the order of a few tenths of a pixel, and these will be propagated into the relation with the lenslet positions. Atmospheric differential refraction has a more pronounced effect, which is discussed in more detail below.

5.1.2. *Atmospheric Differential Refraction*

Atmospheric differential refraction (Filippenko 1982; Roe 2002) presents an additional challenge in finding the exact location of

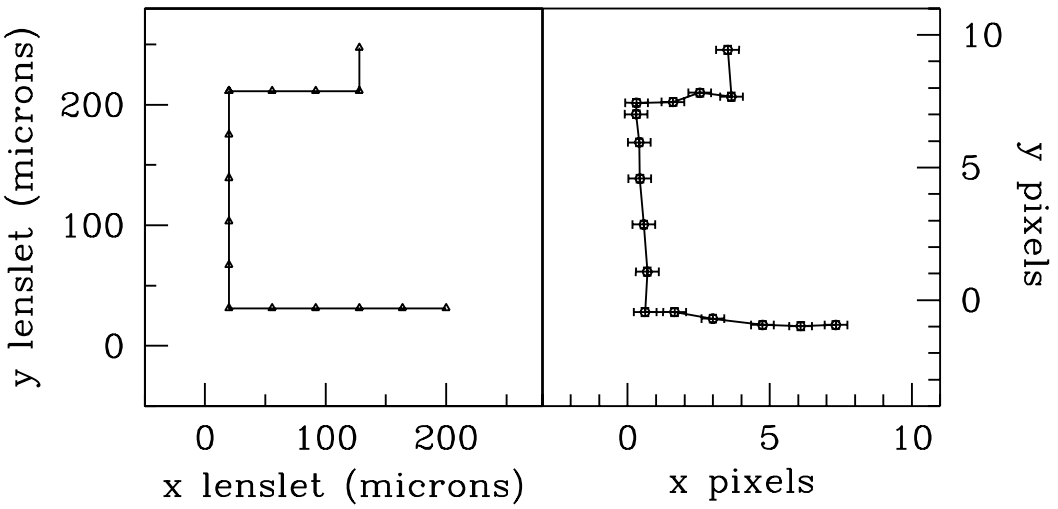

FIG. 9.—Comparison between lenslet motor positions and star pixel locations for HIP 62886, demonstrating the linear relations between the coordinates. One pixel corresponds to approximately 13.5 mas on the sky. There is no significant correlation between the lenslet x and the star y pixel value and between the lenslet y and the x pixel coordinates; these relations have linear correlation coefficients of -0.242 and -0.256, respectively. The error bars in the right panel represent the uncertainties in both the centroiding and the lenslet motor positions; they are in effect the combined errors from both parts of the plot, showing the likely uncertainty in derived star location for a given lenslet position. The error bars shown are approximate and only intended as a guide, but they nevertheless reflect the larger scatter in x than y that is evident in Fig. 8. This is likely to be largely due to a difference in x and y motor hysteresis. The lenslet motor positions shown here are taken from a subset of the observations shown in Fig. 8.

the occulted star. The atmospheric index of refraction is wavelength dependent and so the measured position of an object will change with wave band. Furthermore, this effect is strongly dependent on the air mass through which a source is being observed. At a zenith distance of 10° an object may typically show a ~0.″1 difference between its *H*-band position and its optical position; at 60°, the same star will have a differential displacement of ~0.″7.

Correcting for this effect is important in predicting the occulted star location from feedback from the instrument tip-tilt loop. The star positions are ascertained in *H*-band (1.6 μm) images, while the tip-tilt loop operates in the wavelength range 0.65–1.0 μm. Ideally the tip-tilt loop would operate in the infrared since differential refraction effects are smaller at longer wavelengths, but currently available photon counting devices are not sufficiently sensitive at these wavelengths to adequately measure the small flux that reaches the tip-tilt loop sensors in this instrument. The measured star positions must therefore be corrected for atmospheric refraction before calibrating their relation to the lenslet motor positions. The spectral energy distribution (SED) of the star influences the effective wavelength at which the tip-tilt loop is most sensitive and should be convolved with the photon detector quantum efficiency curve and optical fiber transmission efficiency in order to determine the peak wavelength. However, accurate photometry of the calibration stars in the required 0.65–1.6 μm range does not exist for the binary stars observed to date, so we assume that the tip-tilt loop functions at an effective wavelength of 0.75 μm, corresponding to the peak of the detector efficiency curve.

This approximation will result in a translation of the star-lenslet relation by up to 4 pixels (~54 mas) between observations of different stars due to their differing SEDs. This is witnessed in the data, since although the linear relations for different stars have almost identical gradients, the intercept varies by up to ~100 mas between observations made of different stars and on different nights. This translation is a result of a combination of differential color refraction and an offset between observations in the lenslet positions with respect to the occulting mask hole, due to the motion of other optics in the coronagraph. Both of these effects will be corrected for in future observations, the latter by measuring the locus of the coronagraphic spot in terms of lenslet motor positions with a light source each night, and the former by observing stars with well-defined optical and infrared colors in order to improve the atmospheric differential refraction correction.

Despite this, these two minor calibration issues do not pose a conceptual problem to the principle of using the lenslet motor positions to predict the star location in the image. The results presented here suggest that the occulted star location in the image can be estimated to an accuracy of better than 1 pixel (13.5 mas) from instrument feedback. Although there is uncertainty in the contribution of each source of error to the feedback relation, including that from the mechanical stability of the feedback loop, it is expected that the precision can be increased significantly, possibly to a few tenths of a pixel (~1–5 mas), by improving the image derotation formula and more accurately accounting for refraction effects. This will be achieved with further observations of well-studied calibration binary systems and will reduce the prominence of fake sources in the images obtained from future observing runs.

5.2. *Image Symmetry*

Using only information contained within the image to estimate the occulted star position avoids errors in external information, such as photometry, and in calibrations derived from instrumental configurations. We investigated this type of method by considering the symmetry present in the outer regions of our occulted images. The centroid of the occulted star's PSF does not usually coincide with the actual position of the star, but the symmetry of residual speckles forming the "halo" of the star can provide information on the star's location even when its PSF closer to the core is rather complicated.

A well-corrected, high-Strehl PSF can be expressed as a series expansion of the Fourier transform of phase aberration within the telescope aperture, with alternating symmetric and antisymmetric terms (Sivaramakrishnan et al. 2002; Perrin et al. 2003b). To second order this consists of a symmetric term representing the perfect PSF, an antisymmetric term describing the first-order speckles pinned to the inner Airy rings, and a symmetric second-order component. This model of the PSF is also applicable when a Lyot coronagraph is introduced after the AO system (Bloemhof 2004). The symmetric ideal PSF has its maximum at the image center, whereas antisymmetry causes the first-order pinned speckle term to be zero at the central peak of the PSF. Therefore, to second order, the center of the PSF and the position of the star should coincide with the point in the image about which there is the most symmetry and least antisymmetry. Because the first-order antisymmetric terms are pinned to brighter parts of the PSF, we expect the symmetric second-order halo component to dominate the speckle pattern in regions where the PSF itself is very small, i.e., in the wings of the image. Only the first two terms of the expansion will be significant at the image center where the star is, and a measure of symmetric to antisymmetric power at each pixel should therefore peak at the PSF center and the star position.

This was tested by calculating the ratio of the symmetric to antisymmetric contribution about every point in occulted images of the binary stars HIP 25813 and HIP 62886, in which the true location of the star is known from the binary companion. These calculations are performed by selecting a square box around a given location in the image and computing the symmetric and antisymmetric components of this subregion by, respectively, adding and subtracting the box with itself rotated by 180°. The box was chosen to be 100 pixels square, large enough to cover the central part of the image, but not too large so as to include the binary companion. The results were found to be independent of box size. All pixels inside the box were used in the analysis, including those interior to the occulting spot; these pixels must be considered since the symmetry peak is within this region.

The symmetric contribution, S, is measured as the sum of the pixels in the symmetric part of the box, and the antisymmetric component, A, is twice the sum of the absolute values of the pixels in the antisymmetric part. This process is repeated for every pixel in the image. The ratio of symmetric to total symmetric and antisymmetric contribution, $I = S/(S + A)$, should have its maximum at the center of the PSF and hence indicate the star position. This statistic is chosen rather than S/A since its range is [0, 1]. The ratio calculations were performed on images that had not been flat-fielded, since the presence of the occulting spot in the flat fields introduces false structure into the image center.

Typical results for this method are shown in Figure 10 and can be quantified by calculating the difference between the star position estimated from the symmetry method and that determined from the binary companion. The median of this discrepancy is 37.0 ± 13.7 mas (2.7 ± 1.0 pixels) for the observations of HIP 62886 and 170.6 ± 78.7 mas (12.6 ± 5.8 pixels) for the HIP 25813 images, where the errors are Gaussian standard deviations $\sigma = 1.48\mathrm{MAD}$, with MAD the median of the absolute deviations from the median.

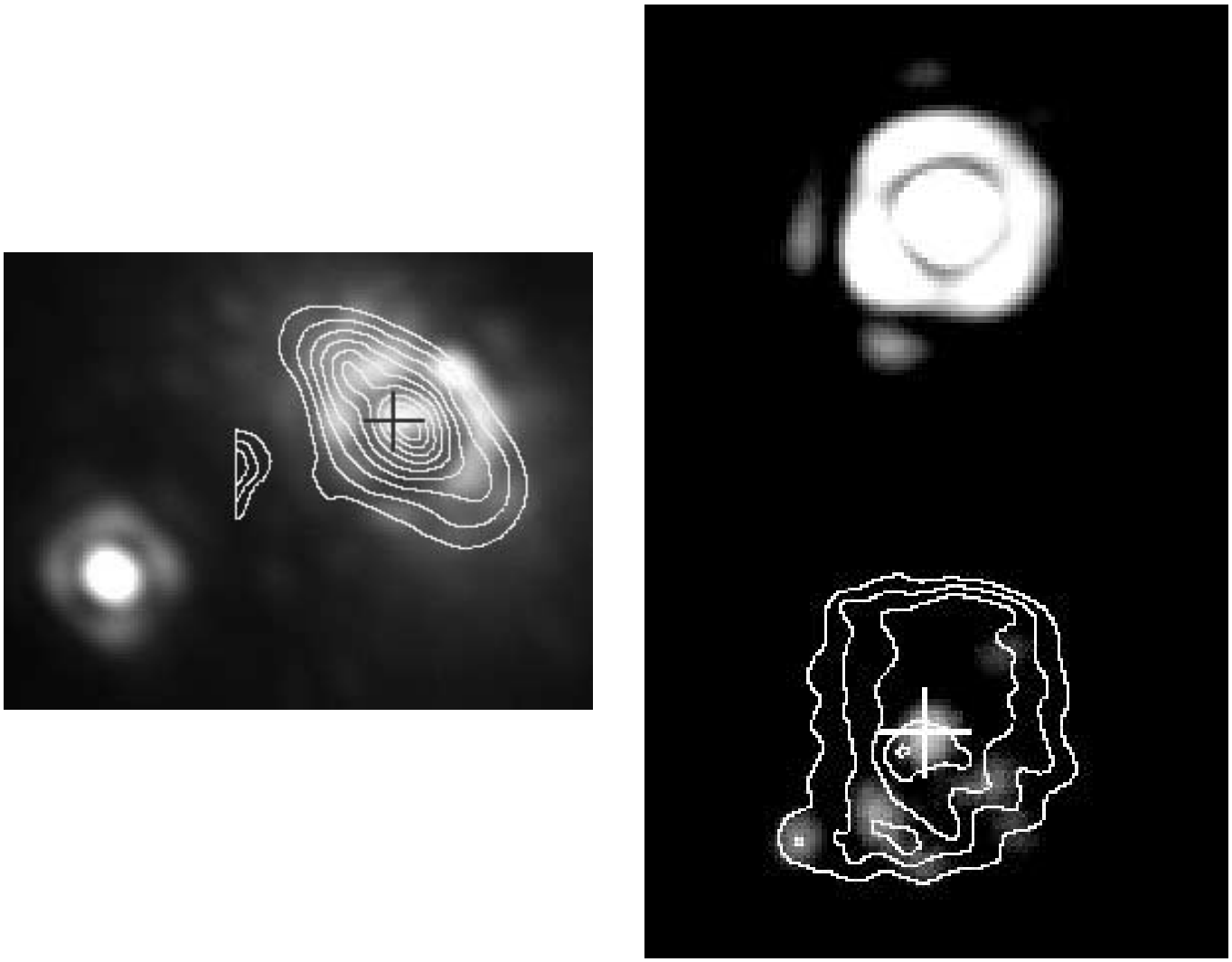

FIG. 10.—Occulted star positions estimated from PSF symmetry (contours show values of the symmetry ratio I) compared to those inferred by the binary companion (*cross*) for typical images of the stars HIP 62886 (*left*) and HIP 25813 (*right*). The symmetry technique works well when the star is well centered on the occulting mask but deteriorates when the star is a larger distance off-axis. In the left panel the star is decentered by $0.65\lambda/D$ and the symmetry contours form a well-defined peak that differs from the binary companion estimate by 38 mas. The right panel shows a more poorly centered configuration ($1.5\lambda/D$), yielding an ill-defined symmetry peak and a discrepancy between the star position estimates of 68 mas. [*See the electronic edition of the Journal for a color version of this figure.*]

The large differences in the accuracy of this technique can at least in part be explained by the off-axis distance of the star in each set of observations. Images in which the star is significantly decentered exhibit little symmetry and would be expected to produce unreliable results with this method, since larger tilt aberrations require more high-order terms in the PSF expansion than offered by the second-order approximation used here. This is borne out by these observations, since in the HIP 25813 images the star was decentered by larger amounts than those of HIP 62886. The offsets from the axis varied between $0.7\lambda/D$ and $2.7\lambda/D$ (64 and 245 mas) for HIP 25813, compared to $0.1\lambda/D$ and $0.9\lambda/D$ (9 and 81 mas) for HIP 62886.

That large aberrations other than tilt degrade the image symmetry is demonstrated in Sivaramakrishnan et al. (2005), who treat the passage of low-order aberrations other than tilt in Lyot coronagraphs, describing first- and second-order effects. They show, for example, that second-order tilt and first-order defocus effects produce a perfectly shaped PSF at the center of the image (i.e., centered behind the focal plane mask) rather than at the star location. When aberrations get large enough that higher order terms become significant, the higher order effects possess mixed symmetries. Even-order terms are symmetric about the stellar location, and odd-order terms antisymmetric. However, the strong presence of both symmetric and antisymmetric terms will remove any useful symmetry from the resultant image.

The effect of centering on the accuracy of the symmetry method is demonstrated in Figure 11. This shows the difference between the true star position (assumed from the binary companion) and the symmetry estimate, as a function of the distance of the star from the occulting spot center. Although there is significant scatter in the plot, in general the symmetry method performs less well for the images of HIP 25813, in which the star is a greater distance off-axis than in the more well-centered HIP 62886 images.

The deviations from this trend indicate that the star-spot alignment is only one factor affecting the accuracy of the symmetry technique in predicting the occulted star position. The quality of the AO correction and significant wave front aberrations other than tilt will also affect the symmetry of the images and hence the reliability of this method, as will real sources that appear close to the occulting spot. Since the accuracy of this method compares poorly with the instrumental feedback approach discussed in

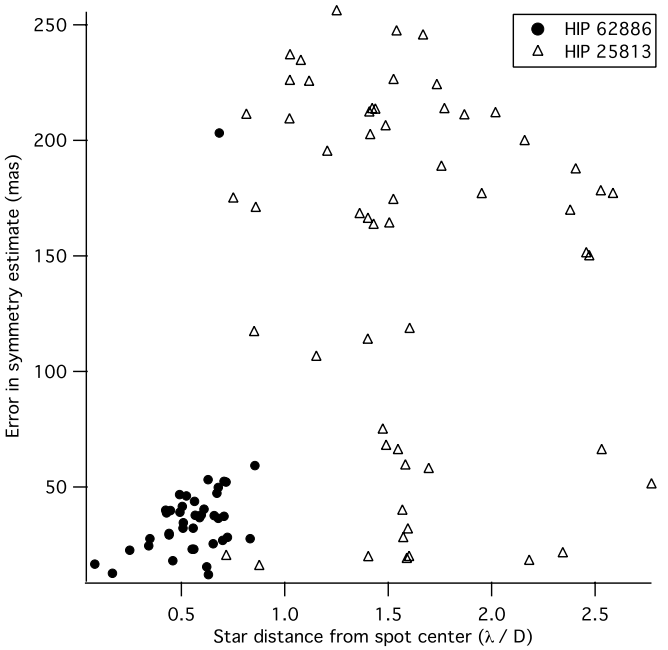

FIG. 11.—Accuracy of predicting the occulted star position from image symmetry as a function of tilt for images of HIP 62886 (*filled circles*) and HIP 25813 (*open triangles*). The error in the symmetry position estimate is derived by assuming that the star's true position is that inferred by the binary companion and is plotted against the distance of the star from the spot center. The more poorly centered HIP 25813 images on the whole exhibit lower accuracy of the symmetry estimate than the more well-centered images of HIP 62886. There is poor correlation and several departures from this predominant trend, however, suggesting that other factors, such as the quality of the wave front correction, also affect the performance of the symmetry technique. In addition, errors in the assumed star position and image derotation will add further scatter to this plot. [*See the electronic edition of the Journal for a color version of this figure.*]

§ 5.1 and appears to be sensitive to centering and image quality, we disregard this technique for determining the star position in occulted images but note that it may have uses in other applications.

6. SUMMARY

AO coronagraphy will be central to many future programs aimed at the direct imaging of high-contrast companions to nearby stars. Such projects face many well-documented optomechanical challenges, but of equal importance is the data analysis. While coronagraphic theory and simulations are developing, significant effort is required to attain a greater empirical understanding of the highly complex coronagraphic images these experiments will produce. Actual high-Strehl coronagraphic data from current instruments provide a means to this understanding, and these projects are important as test beds for future instrumentation in addition to their immediate scientific goals. Future coronagraphs such as the *Terrestrial Planet Finder-Coronagraph* (Stapelfeldt et al. 2005) will require more sophisticated designs than the hard-edged Lyot coronagraph employed in these tests, but the issues discussed here are nevertheless relevant and important to the next generation of instruments.

The issue of determining the location of the occulted star in images is an important challenge in the analysis of coronagraphic data and should be carefully considered during instrument design. We have considered three approaches to this problem for the case of the Lyot Project coronagraph, predicting the star position from the image centroid, image symmetry, and instrument feedback. The first two methods yield median accuracies of 74 and 37 mas, respectively, in recovering the star position in images of HIP 62886, whereas the feedback from the tip-tilt loop provides accuracies of better than 13.5 mas. Furthermore, the centroiding and the symmetry approach are highly dependent on factors such as wave front correction quality and the subsection of image chosen for the analysis. Instrument feedback provides a more reliable solution, on the other hand, which should achieve even better accuracy with further refinement. This is the technique that will be employed in the data analysis for the Lyot Project instrument, and although the details presented here are unique to this instrument, the principle is generally applicable to any AO coronagraph. Other instrument architectures may present additional challenges from instrument flexure and from alternative tip-tilt loop configurations, but all high dynamic range coronagraphs will require some form of active alignment of the star with the occulting spot. All such instruments will therefore yield some form of tip-tilt feedback that can be used to infer the star position with respect to the occulting spot. There will of course be many alternative methods for predicting the occulted star location in coronagraphic images, but our experience from the Lyot Project coronagraph suggests that given the variability and complexity of the data, it is preferable to use calibrated internal metrology as an indicator of the star position rather than the information contained within the image.

The authors are grateful to the anonymous referee for their important contributions and particularly for their comments regarding the significance of these results in a wider context.

The Lyot Project is grateful to the Cordelia Corporation, Hilary and Ethel Lipsitz, the Vincent Astor Fund, Judy Vale, and an anonymous donor, who helped to initiate the project.

The Lyot Project is based on work supported by the National Science Foundation under grants 0334916, 0215793, and 0520822, as well as grant NNG05GJ86G from the National Aeronautics and Space Administration under the *Terrestrial Planet Finder* Foundation Science Program. The Lyot Project gratefully acknowledges the support of the US Air Force and NSF in creating the special Advanced Technologies and Instrumentation opportunity that provides access to the AEOS telescope. Eighty percent of the funds for that program are provided by the US Air Force. This work has also been supported by the National Science Foundation Science and Technology Center for Adaptive Optics, managed by the University of California at Santa Cruz under cooperative agreement AST 98-76783.

A. P. D. and R. S. are supported by NASA Michelson Postdoctoral Fellowships, and M. D. P. is supported by a Michelson Graduate Fellowship, under contract with the Jet Propulsion Laboratory (JPL) funded by NASA. JPL is managed for NASA by the California Institute of Technology. L. C. R. is funded by the Air Force Research Laboratory's Directed Energy Directorate (contract F29601-00-D-0204). A. S. and R. B. M. acknowledge support from the Space Telescope Science Institute Director's Discretionary Fund.

The authors are grateful to the following people for invaluable contributions to the Lyot Project: Jacob Mey, Michael Benedetto, Dragoslav Scepanovic, and Liza Ezbiansky.

This research has made use of the SIMBAD database, operated at CDS, Strasbourg; the Washington Double Star Catalog, maintained at the US Naval Observatory; and STSDAS and PyRAF, which are products of the Space Telescope Science Institute, operated by AURA for NASA.

REFERENCES

Aime, C., & Soummer, R. 2004, ApJ, 612, L85
Aime, C., Soummer, R., & Ferrari, A. 2002, A&A, 389, 334
Anderson, J., & King, I. R. 2000, PASP, 112, 1360
Bloemhof, E. E. 2003, ApJ, 582, L59
———. 2004, ApJ, 610, L69
Bloemhof, E. E., Dekany, R. G., Troy, M., & Oppenheimer, B. R. 2001, ApJ, 558, L71
Christou, J. C., Pugliese, G., Köhler, R., & Drummond, J. D. 2004, PASP, 116, 734
Christou, J. C., Steinbring, E., Faber, S. M., Gavel, D. T., Patience, J., & Gates, E. L. 2003, Proc. SPIE, 4839, 846
Drummond, J., Milster, S., Ryan, P., & Roberts, L. C., Jr. 2003, ApJ, 585, 1007
Fabricius, C., & Makarov, V. V. 2000, A&A, 356, 141
Filippenko, A. V. 1982, PASP, 94, 715
Heintz, W. D. 1997, ApJS, 111, 335
Hinkley, S., et al. 2006, ApJ, in press
Krist, J. E., Golimowski, D. A., Schroeder, D. J., & Henry, T. J. 1998, PASP, 110, 1046
Kuchner, M. J., Crepp, J., & Ge, J. 2005, ApJ, 628, 466
Kuchner, M. J., & Traub, W. A. 2002, ApJ, 570, 900
Lazorenko, P. F., & Lazorenko, G. A. 2004, A&A, 427, 1127
Lindegren, L. 1980, A&A, 89, 41
Lloyd, J. P., & Sivaramakrishnan, A. 2005, ApJ, 621, 1153
Lyot, B. 1939, MNRAS, 99, 580
Macintosh, B. A., et al. 2004, Proc. SPIE, 5490, 359
Makidon, R. B., Sivaramakrishnan, A., Perrin, M. D., Roberts, L. C., Jr., Oppenheimer, B. R., Soummer, R., & Graham, J. R. 2005, PASP, 117, 831
Marcy, G. W., & Butler, R. P. 1996, ApJ, 464, L147
Mayor, M., & Queloz, D. 1995, Nature, 378, 355
Mighell, K. J. 2005, MNRAS, 361, 861
Nakajima, T. 1994, ApJ, 425, 348
Oppenheimer, B. R., et al. 2004, Proc. SPIE, 5490, 433
Perrin, M. D., Graham, J. R., Trumpis, M., Kuhn, J., Whitman, K., Coulter, R., Lloyd, J. P., & Roberts, L. C., Jr. 2003a, in Proceedings of the AMOS Technical Conference, ed. P. W. Kervin & J. L. Africano (Kihei: Maui Economic Development Board)
Perrin, M. D., Sivaramakrishnan, A., Makidon, R. B., Oppenheimer, B. R., & Graham, J. R. 2003b, ApJ, 596, 702
Racine, R., Walker, G. A. H., Nadeau, D., Doyon, R., & Marois, C. 1999, PASP, 111, 587
Roberts, L. C., Jr., & Neyman, C. R. 2002, PASP, 114, 1260
Roberts, L. C., Jr., et al. 2005, AJ, 130, 2262
Roe, H. G. 2002, PASP, 114, 450
Seymour, D., & Hartkopf, W. I. 1999, IAU Commission on Double Stars, 139, 2
Shaklan, S. B., & Green, J. J. 2005, ApJ, 628, 474
Sivaramakrishnan, A., Koresko, C. D., Makidon, R. B., Berkefeld, T., & Kuchner, M. J. 2001, ApJ, 552, 397
Sivaramakrishnan, A., Lloyd, J. P., Hodge, P. E., & Macintosh, B. A. 2002, ApJ, 581, L59
Sivaramakrishnan, A., Soummer, R., Sivaramakrishnan, A. V., Lloyd, J. P., Oppenheimer, B. R., & Makidon, R. B. 2005, ApJ, 634, 1416
Sivaramakrishnan, A., Weymann, R. J., & Beletic, J. W. 1995, AJ, 110, 430
Soummer, R. 2005, ApJ, 618, L161
Stapelfeldt, K., Beichman, C., & Kuchner, M. 2005, NewA Rev., 49, 396
Stetson, P. B. 1987, PASP, 99, 191
———. 1992, in ASP Conf. Ser. 25, Astronomical Data Analysis Software and Systems I, ed. D. M. Worrall, C. Biemesderfer, & J. Barnes (San Francisco: ASP), 297
Véran, J.-P., & Durand, D. 2000, in ASP Conf. Ser. 216, Astronomical Data Analysis Software and Systems IX, ed. N. Manset, C. Veillet, & D. Crabtree (San Francisco: ASP), 345